Resting state global brain activity induces bias in fMRI motion estimates

Yixiang Mao[a,b,*], Conan Chen[a,b], Truong Nguyen[b], Thomas T. Liu[a,c,*]

[a] *Center for Functional MRI, University of California San Diego, 9500 Gilman Drive MC 0677, La Jolla, CA 92093*
[b] *Departments of Electrical and Computer Engineering, University of California San Diego, 9500 Gilman Drive, La Jolla, CA 92093*
[c] *Departments of Radiology, Psychiatry, and Bioengineering, University of California San Diego, 9500 Gilman Drive, La Jolla, CA 92093*

Abstract

Head motion is a significant source of artifacts in resting-state fMRI (rsfMRI) studies and has been shown to affect resting-state functional connectivity (rsFC) measurements. In many rsfMRI studies, motion parameters estimated from volume registration are used to characterize head motion and to mitigate motion artifacts in rsfMRI data. While prior task-based fMRI studies have shown that task-evoked brain activations may induce temporally correlated bias in the motion estimates, resulting in artificial activations after registration, relatively little is known about neural-related bias in rsfMRI motion parameters. In this study, we demonstrate that neural-related bias exists in rsfMRI motion estimates and characterize the potential effects of the bias on rsFC estimates. Using a public multi-echo rsfMRI dataset, we use the differences between motion estimates from the first echo and second echo data as a measure of neural-induced bias. We show that the resting-state global activity of the brain, as characterized with the global signal (GS), induces bias in the motion estimates in the y- and z-translational axes. Furthermore, we demonstrate that the GS-related bias reflects superior-inferior and anterior-posterior asymmetries in the GS beta coefficient map. Finally, we demonstrate that regression with biased motion estimates can negatively bias rsFC estimates and reduce rsFC differences between young and old subjects.

Keywords: Resting state fMRI, multi-echo fMRI, global signal, motion parameters, resting-state functional connectivity

*Corresponding Authors
Email addresses: `y1mao@ucsd.edu` (Yixiang Mao), `ttliu@ucsd.edu` (Thomas T. Liu)

1. Introduction

Head motion is a major source of artifacts in fMRI data, and motion estimates from data registration are commonly used to characterize and mitigate motion-related artifacts (Friston et al., 1996; Power et al., 2012; Satterthwaite et al., 2012; Dijk et al., 2012; Yan et al., 2013; Power et al., 2014, 2015). Prior task-based fMRI studies demonstrated that task-evoked brain activations can induce bias in motion estimates that is temporally correlated with brain activations (Freire and Mangin, 2001; Freire et al., 2002). In contrast, relatively little is known about neural-related bias in motion estimates from resting-state fMRI (rsfMRI) data.

Detecting such bias is challenging due to the absence of ground truth head motion and neural signals in rsfMRI studies. To first order, fMRI signal changes resulting from head motion and neural activity can be distinguished based on their dependence on echo time (TE): neural activity causes TE-dependent blood-oxygen-level-dependent (BOLD) fluctuations, whereas head motion largely contributes to TE-independent non-BOLD signal changes. Taking advantage of these differences, prior studies have demonstrated that BOLD and non-BOLD signals can be distinguished using multi-echo fMRI (MEfMRI) that acquires data at different TEs (Buur et al., 2009; Bright and Murphy, 2013; Kundu et al., 2012, 2017). For example, Burr et al. effectively used the first echo data acquired at a short TE with minimal BOLD-weighting to model and correct for the motion artifacts in the BOLD-weighted second echo data (Buur et al., 2009).

Burr's findings imply that it may be feasible to identify neural-related bias by comparing motion estimates obtained from the first and second echo data. Since head motion primarily results in TE-independent signal changes, its effects should be captured in the motion estimates derived from both the first and second echo data. In contrast, there is typically minimal BOLD weighting in the first echo data but strong BOLD weighting in the second echo data. As prior work has shown that a higher level of brain activation can lead to greater bias in motion estimates (Freire and Mangin, 2001; Freire et al., 2002), potential neural-related bias should exhibit greater magnitude in the motion estimates from the second echo data as compared to those from the first echo data. Taken together, potential neural-related bias may be isolated from head motion by examining the difference between the motion estimates obtained from the first and second echo data.

Prior task-based fMRI studies have shown that brain activations with a larger spatial extent can lead to a higher level of bias in the motion estimates (Freire and Mangin, 2001; Freire et al., 2002).

This finding motivates us to examine whether global brain activity in rsfMRI leads to bias in the motion estimates. In this study, we used the global signal (GS), calculated as the mean fMRI signal over the voxels within the brain, as a proxy for global brain activity. While the interpretation of the GS is still controversial (reviewed in (Liu and Falahpour, 2020)), there is growing evidence suggesting that the GS is linked to global neural activity (Wong et al., 2013, 2016; Falahpour et al., 2018; Liu et al., 2018; Gu et al., 2021).

In this work, we characterized the bias in rsfMRI motion parameters as estimated by AFNI *3dvolreg*. Furthermore, we investigated the consequences of using biased estimates as regressors in resting-state functional connectivity (rsFC) analyses.

2. Methods

2.1. Subjects and MEfMRI data acquisition

In this study, we used a public dataset (denoted as the Cornell-York dataset and described in (Setton et al., 2022)) downloaded from OpenNeuro (dataset ds003592). The Cornell-York dataset includes multi-echo fMRI data collected from 301 healthy subjects (181 younger and 120 older adults). The data from 238 subjects were acquired on a 3T GE Discovery MR750 MRI scanner with a 32-channel head coil. The data from the remaining 63 subjects were collected on a 3T Siemens Trio MRI scanner with a 32-channel head coil. For each subject, two 10-min resting-state runs were acquired using an ME EPI sequence on the GE scanner (204 volumes; TR=3000 ms; TE=$13.7, 30, 47$ ms; flip angle=83°; FOV=210 mm; voxel size=$3\times3\times3$ mm^3; matrix size=$72\times72\times46$; 2.5×SENSE acceleration; phase encoding direction: A-P) or on the Siemens scanner (200 volumes; TR=3000 ms; TE=$14, 29.96, 45.92$ ms; flip angle=83°; FOV=216 mm; voxel size=$3.4\times3.4\times3$ mm^3; matrix size=$64\times64\times43$; 3×GRAPPA acceleration; phase encoding direction: A-P). The subjects were instructed to stay awake and lie still with their eyes open during the scans.

2.2. Data preprocessing

AFNI was used for data preprocessing (Cox, 1996). The fMRI data from the first and second echoes were used and denoted as e1 and e2, respectively. The data were first reoriented to Right-Anterior-Inferior (RAI) orientation (AFNI *3dresample -orient RAI*), and the first 6 TRs of the data were discarded to allow magnetization to reach a steady state. For each run and each echo, the data were normalized so that

the mean signal over all voxels and all volumes was equal to 100. Since the normalization is equivalent to multiplication by a global scaling factor, the spatial and temporal information of the data in each run is preserved.

2.3. Calculation of the motion estimates and global signal

In this study, we examined the motion estimates from AFNI *3dvolreg* (Cox and Jesmanowicz, 1999) using the first volume as the reference volume. The default weights used in registration were disabled by feeding an all-ones image to the `-weight` option. This approach weights all voxels equally during registration. For each run, the motion was estimated using both the e1 and e2 data. Then, the motion parameters were multiplied by -1 to represent the movement of the volumes as compared to the reference volume (see Appendix A).

For each run, the global signal (GS) was calculated from the unregistered e2 data. Before calculating the GS, each voxel's signal was converted to a percent change signal. Then, the GS was computed by averaging over all voxels within the brain (brain masks were formed by AFNI *3dAutomask*). Finally, the mean and the linear and quadratic trends were regressed out from the motion estimates and GS.

2.4. Identifying BOLD-weighted GS bias in the motion estimates

To characterize BOLD-weighted GS bias in the motion estimates, we considered a simple signal model for the e1 and e2 motion estimates. Let $\boldsymbol{m}_{e1} \in \mathbb{R}^{K\times 1}$ and $\boldsymbol{m}_{e2} \in \mathbb{R}^{K\times 1}$ represent the motion estimates of one motion axis each from e1 and e2, respectively, where K is the number of volumes. We model the motion estimates as the weighted sum of head motion, BOLD-weighted GS bias and estimation error,

$$\begin{aligned} \boldsymbol{m}_{e1} &= \alpha_{e1}\boldsymbol{m}_h + \beta_{e1}\mathrm{TE}_1\boldsymbol{g}_s + \boldsymbol{\epsilon}_{e1} \\ \boldsymbol{m}_{e2} &= \alpha_{e2}\boldsymbol{m}_h + \beta_{e2}\mathrm{TE}_2\boldsymbol{g}_s + \boldsymbol{\epsilon}_{e2} \end{aligned} \tag{1}$$

where $\boldsymbol{m}_h \in \mathbb{R}^{K\times 1}$ represents head motion, α_{ei} is the regression weight corresponding to head motion for the ith echo, $\boldsymbol{g}_s \in \mathbb{R}^{K\times 1}$ is the GS, TE_1 and TE_2 are the first and second echo times, respectively, β_{ei} is the regression weight of the BOLD-weighted GS bias for the ith echo and $\boldsymbol{\epsilon}_{ei} \in \mathbb{R}^{K\times 1}$ is the estimation error for the ith echo. With the above model, subtracting $\boldsymbol{m}_{e1}$ from $\boldsymbol{m}_{e2}$ yields

$$\Delta\boldsymbol{m} = \boldsymbol{m}_{e2} - \boldsymbol{m}_{e1} = (\alpha_{e2} - \alpha_{e1})\boldsymbol{m}_h + (\beta_{e2}\mathrm{TE}_2 - \beta_{e1}\mathrm{TE}_1)\boldsymbol{g}_s + \boldsymbol{\epsilon}_{e2} - \boldsymbol{\epsilon}_{e1} \tag{2}$$

Since prior findings suggest that head motion can be accurately estimated from both e1 and e2 data (Buur et al., 2009; Speck and Hennig, 2001), we assume that $\alpha_{e1} = \alpha_{e2}$, yielding

$$\Delta \boldsymbol{m} = (\beta_{e2}\mathrm{TE}_2 - \beta_{e1}\mathrm{TE}_1)\boldsymbol{g_s} + \boldsymbol{\epsilon}_{e2} - \boldsymbol{\epsilon}_{e1} \tag{3}$$

Note that $\Delta \boldsymbol{m}$ isolates BOLD-weighted GS bias from head motion. Therefore, we can examine the presence of potential bias by assessing the significance of the correlations between $\Delta \boldsymbol{m}$ and the GS. For each run and motion axis, we calculated the correlation between $\Delta \boldsymbol{m}$ and the GS (denoted as $r(\Delta \boldsymbol{m}, \mathrm{GS})$) and assessed the statistical significance of $r(\Delta \boldsymbol{m}, \mathrm{GS})$ values on a per-run basis using empirical null distributions. For each motion axis, a null distribution was formed by calculating $r(\Delta \boldsymbol{m}, \mathrm{GS})$ values using all possible permutations across runs, i.e. pairing the GS from one run to $\Delta \boldsymbol{m}$ from other runs and looping over all runs. The resulting null distributions consisted of 361,802 samples. Then, for each motion axis, we used the null distribution to compute the two-sided p-value associated with the $r(\Delta \boldsymbol{m}, \mathrm{GS})$ value calculated from each run's measured data. A p-value threshold of 0.05 was divided by 602 (the number of runs) to correct for multiple comparisons, and the Bonferroni corrected threshold was used to determine the significant correlations. Finally, we calculated the percentage of runs that show significant $r(\Delta \boldsymbol{m}, \mathrm{GS})$ values for each motion axis.

In this study, we used the GS to represent the global activity of the brain. To reduce the potential effect of motion artifacts in the GS, we repeated the above analysis after regressing out the e1 motion regressors from both the GS and $\Delta \boldsymbol{m}$. The e1 motion regressors included the six motion parameters estimated from the e1 data and their first derivatives.

2.5. Spatial maps underlying $r(\Delta \boldsymbol{m}, GS)$

To provide insight into the mechanisms underlying BOLD-weighted GS bias, we derived an empirical approximation for $r(\Delta \boldsymbol{m}, \mathrm{GS})$. As shown in Appendix C,

$$r(\Delta \boldsymbol{m}, \mathrm{GS}) \approx \frac{\|\boldsymbol{g_s}\|}{\|\Delta \boldsymbol{m}\|} \left(\frac{\boldsymbol{\beta}^T_{\boldsymbol{g}_s, e2} \boldsymbol{d}_{e2}}{\|\boldsymbol{d}_{e2}\|^2} - \frac{\boldsymbol{\beta}^T_{\boldsymbol{g}_s, e1} \boldsymbol{d}_{e1}}{\|\boldsymbol{d}_{e1}\|^2} \right) \tag{4}$$

where $\boldsymbol{\beta}_{\boldsymbol{g}_s, ei} \in \mathbb{R}^{N \times 1}$ is the GS beta coefficient map for the ith echo, $\boldsymbol{d}_{ei} \in \mathbb{R}^{N \times 1}$ is the spatial derivative image with respect to (w.r.t.) one motion axis of the ith echo, N is the number of voxels and $\|\cdot\|$ denotes the $L2$-norm. For each run, the GS beta coefficient map $\boldsymbol{\beta}_{\boldsymbol{g}_s, ei} = \frac{\boldsymbol{Y}_{ei}\boldsymbol{g}_s}{\|\boldsymbol{g}_s\|^2}$ was calculated from the linear fit of the GS to the unregistered functional data $\boldsymbol{Y}_{ei} \in \mathbb{R}^{N \times K}$ of the ith echo.

We calculated the spatial derivative images w.r.t. motion axes following the calculation in AFNI *3dvolreg*. For each run and each echo, the spatial derivative images were calculated based on the reference volume used in motion estimation. Denoting the reference image of the ith echo as $\boldsymbol{y}_{r,ei} \in \mathbb{R}^{N\times 1}$, the spatial derivative image of the ith echo w.r.t the jth motion axis was calculated as

$$\boldsymbol{d}_{ei,j} = \frac{T_j(\boldsymbol{y}_{r,ei}, \epsilon_j) - T_j(\boldsymbol{y}_{r,ei}, -\epsilon_j)}{2\epsilon_j}, \quad i = 1, 2, j \in \{\text{Rx, Ry, Rz, Tx, Ty, Tz}\} \tag{5}$$

where $T_j : \mathbb{R}^{N\times 1} \to \mathbb{R}^{N\times 1}$ is the function that transforms the reference volume along the jth motion axis, ϵ_j is the transformation parameter, Rx, Ry and Rz represent x-, y- and z-rotation, respectively and Tx, Ty, Tz represent x-, y- and z-translation, respectively. When calculating the spatial derivative images, the transformation was performed with AFNI *3drotate -heptic*. For the translational motion axes, ϵ was set to 2.1 mm. For the rotational motion axes, ϵ was set to 0.4°. The exact values were used in AFNI *3dvolreg* when creating the derivative images and were calculated based on the spatial resolution of the functional data.

2.6. Effect of the bias on ROI-ROI FC via motion regression

In this work, we investigated the effect of regression with biased motion estimates on rsFC estimates between nodes within the default mode network (DMN) and task positive network (TPN). The regions of interest (ROIs) within these networks were defined in (Dijk et al., 2010), with four ROIs in the DMN (the posterior cingulate cortex (PCC), lateral parietal cortex (LatPar), medial prefrontal cortex (mPFC) and Hippocampal formation (HF)) and three ROIS in the TPN (frontal eye field (FEF), intraparietal cortex (IPS) and middle temporal area (MT+)). Seed ROIs were created using a sphere with a radius of 12 mm centered about each seed coordinate. The left and right ROIs were combined to form bilateral ROIs. Prior to averaging signals within each ROI, the e2 data after volume registration were transferred to MNI space and spatially smoothed with a 4mm FWHM Gaussian kernel.

To reduce the confounding effects of head motion, motion censoring was performed before motion regression. For each run, framewise displacement (FD) was calculated based on six motion parameters estimated from the e1 data (the calculation of FD follows the description in (Power et al., 2012)). Volumes with FD values larger than 0.2 mm were censored. We showed in the supplementary materials (Fig. S4 and S5) that motion censoring has little impact on the effect of regression with biased motion estimates on rsFC.

After motion censoring, we calculated and compared the ROI-ROI FC after e2 and e1 motion regression to assess the effect of potential bias on FC analysis. For each ROI, the ROI-based seed signal was calculated by averaging the percent change BOLD signal over the voxels in that ROI. Then, the motion regressors, including the six motion parameters and their first derivatives were regressed out from the ROI signals. For each pair of ROIs, the ROI-ROI FC was computed as Pearson's correlation coefficients between the ROI average signals. Correlation values were converted to z-scores using the Fisher-z transformation. The differences in the ROI-ROI FC calculated after e2 and e1 motion regression were calculated to assess the effect of the bias on FC. The e2-e1 differences in r-values and z-scores were denoted as Δr and Δz, respectively.

Furthermore, we examined the effect of the bias on FC within four groups of runs based on levels of head motion and GS. For each run, the level of head motion was measured by the mean FD value calculated by averaging over the FD values across time. The level of the GS was measured by the GS amplitude (aGS) computed as the standard deviation of the GS after motion censoring. All the runs were first divided into two groups based on their mean FD values. Runs with mean FD values larger than the group median were classified as high motion runs and the remaining runs were classified as low motion runs. Then, within each FD-based group, the runs were further divided into two groups based on aGS. Runs with aGS values larger than the group median were classified as high aGS runs and the remaining runs were classified as low aGS runs. Consequently, we formed four groups of runs: 1) low motion and high aGS runs, (2) low motion and low aGS runs, (3) high motion and high aGS runs and (4) high motion and low aGS runs. A one-way ANOVA was calculated on mean Δz over all ROI pairs to assess whether there was a group effect. Post-hoc two-sample t-tests were calculated to characterize the differences between pairs of groups.

Additionally, to verify that the effect of the bias on FC was dominated by the motion estimates from the axes where we found GS-induced bias, we evaluated the effect of two subsets of motion regressors. One of the subsets included the motion estimates and their first derivatives from the Ty and Tz axes (where we found GS-induced bias), while the other subset included the motion regressors from the other four motion axes, where minimal GS-induced was observed.

2.7. Effect of the bias on young vs. old group-level FC analysis

In this study, we used a public dataset consisting of young and old subjects (181 younger and 120 older adults as described in Setton et al. (2022)). We first examined whether the bias in motion estimates

affects the ROI-ROI FC of the young and old subjects differently by comparing Δr and Δz between the young and old runs. Furthermore, we investigated if the bias alters the group-level FC analysis between the young and old subjects. For each pair of ROIs, the significance of the FC differences between the young and old subjects was assessed by a permutation test with 1×10^7 random permutations to allow us to examine the commonly used p-values thresholds of 0.01, 1×10^{-3} and 1×10^{-6}. Also, the effect size of the differences was measured with Cohen's d. The FC differences and the significance and effect size of the differences calculated after e1 and e2 motion regression were compared.

3. Results

3.1. Examples of the GS and motion estimates

Fig. 1 (a,b) show the motion estimates in the Tz axis, including $\boldsymbol{m}_{e1}$ (blue), $\boldsymbol{m}_{e2}$ (green) and $\Delta\boldsymbol{m}$ (red) from two example runs with (a) low and (b) high levels of motion. Note that for the high motion run, $\boldsymbol{m}_{e1}$ and $\boldsymbol{m}_{e2}$ are plotted at 1/20th scale to facilitate comparison with $\boldsymbol{m}_{e1}$ and $\boldsymbol{m}_{e2}$ from the low motion run. As shown in these subfigures, $\Delta\boldsymbol{m}$ estimates from both runs fluctuate in a similar range from -0.05 to 0.05 mm (std($\Delta\boldsymbol{m}$) = 0.017 and 0.025 for the low and high motion runs, respectively). In contrast, the standard deviations of $\boldsymbol{m}_{e1}$ and $\boldsymbol{m}_{e2}$ from the high motion run (std($\boldsymbol{m}_{e1}$) = 0.583, std($\boldsymbol{m}_{e2}$) = 0.602) are an order of magnitude larger than the standard deviations of $\boldsymbol{m}_{e1}$ and $\boldsymbol{m}_{e2}$ from the low motion run (std($\boldsymbol{m}_{e1}$) = 0.027, std($\boldsymbol{m}_{e2}$) = 0.034).

Fig. 1 (c) and (d) show the GS and $\Delta\boldsymbol{m}$ from the low motion and high motion runs, respectively. For the low motion run, $\Delta\boldsymbol{m}$ covaries with the GS throughout the run, leading to a strong $r(\Delta\boldsymbol{m}, \mathrm{GS})$ of 0.93. The high motion run shows a weaker $r(\Delta\boldsymbol{m}, \mathrm{GS})$ of 0.34 as compared to the low motion run, and reflects motion artifacts in the GS. After motion regression (panels e and f), the $r(\Delta\boldsymbol{m}, \mathrm{GS})$ for the high motion run increases to 0.62, while the $r(\Delta\boldsymbol{m}, \mathrm{GS})$ of the low motion run remains at a high value of 0.92, suggesting that the relation between the GS and $\Delta\boldsymbol{m}$ is enhanced when motion artifacts are minimized.

3.2. Significance testing for $r(\Delta\boldsymbol{m}, GS)$ values

To examine the presence of BOLD-weighted GS bias over runs and motion axes, we assessed the significance of $r(\Delta\boldsymbol{m}, \mathrm{GS})$ values on a per-run and per-axis basis using permutation-based empirical null distributions. Fig. 2 shows two-sided violin plots of the distributions of $r(\Delta\boldsymbol{m}, \mathrm{GS})$ values (blue) and the empirical null distributions (green) for all six motion axes (a) before and (b) after e1 motion regression.

The blue solid lines and circles represent the median values for each distribution of measured $r(\Delta\boldsymbol{m}, \mathrm{GS})$ values. The dashed lines represent the $r(\Delta\boldsymbol{m}, \mathrm{GS})$ values corresponding to a Bonferroni corrected p-value threshold of 0.05 (two-sided) assessed from the empirical null distributions. The dark red square markers represent the percentages of runs showing $r(\Delta\boldsymbol{m}, \mathrm{GS})$ values that are significantly different from zero.

In the Tz axis, 61.1% and 69.3% of the runs show significant positive $r(\Delta\boldsymbol{m}, \mathrm{GS})$ values before and after e1 motion regression, respectively. The group median $r(\Delta\boldsymbol{m}, \mathrm{GS})$ value increases from 0.55 to 0.58 after e1 motion regression. Remarkably, 96 out of 602 total runs show $r(\Delta\boldsymbol{m}, \mathrm{GS})$ values larger than 0.8 after e1 motion regression. In the Ty axis, 30.6% and 38.2% of the runs show significant $r(\Delta\boldsymbol{m}, \mathrm{GS})$ values before and after e1 motion regression, respectively. The group median $r(\Delta\boldsymbol{m}, \mathrm{GS})$ value increases from 0.29 to 0.34 after e1 motion regression. Fig. S1 and S2 show examples of the GS and the motion estimates, including $\boldsymbol{m}_{e1}$, $\boldsymbol{m}_{e2}$ and $\Delta\boldsymbol{m}$ in the Tz and Ty axes, respectively. Together, these findings indicate the presence of BOLD-weighted GS bias in the Tz and Ty motion estimates.

For the other motion axes (Rx, Ry, Rz and Tx), the percent of significant $r(\Delta\boldsymbol{m}, \mathrm{GS})$ values fluctuates around 5%, ranging from 1.2% to 6.6%, indicating minimal BOLD-weighted GS bias for these axes.

3.3. Visualizing the spatial maps underlying $r(\Delta\boldsymbol{m}, GS)$ values

In the previous section, BOLD-weighted GS bias in the motion estimates was identified by examining the temporal correlations between the GS and $\Delta\boldsymbol{m}$. Furthermore, as described in Eq. 4, $r(\Delta\boldsymbol{m}, \mathrm{GS})$ can be approximated as multiplying the difference of $\frac{\boldsymbol{\beta}_{\boldsymbol{g}_s}^T \boldsymbol{d}}{\|\boldsymbol{d}\|^2}$ from e2 and e1 by a scaling factor $\frac{\|\boldsymbol{g}_s\|}{\|\Delta\boldsymbol{m}\|}$. The approximation provides us a unique angle to interpret the GS bias by looking at the relation of the $\boldsymbol{\beta}_{\boldsymbol{g}_s}$ and $\boldsymbol{d}$ spatial maps. Fig. 3 visualizes $\boldsymbol{\beta}_{\boldsymbol{g}_s}$, $\frac{\boldsymbol{d}}{\|\boldsymbol{d}\|^2}$, $\frac{\boldsymbol{\beta}_{\boldsymbol{g}_s} \odot \boldsymbol{d}}{\|\boldsymbol{d}\|^2}$, and the $\frac{\boldsymbol{\beta}_{\boldsymbol{g}_s} \odot \boldsymbol{d}}{\|\boldsymbol{d}\|^2}$ difference maps in the Tz and Tx axes from an example run, where $\odot$ represents element-wise multiplication.

In the Tz axis, $\frac{\boldsymbol{d}}{\|\boldsymbol{d}\|^2}$ exhibits high positive and negative values at the superior and inferior edges of the brain, respectively, whereas $\boldsymbol{\beta}_{\boldsymbol{g}_s}$ exhibits positive values across the cortex, including the superior edge of the brain but exhibits relatively low values (approaching zero) along the inferior edge. As a result, most of the high values in $\frac{\boldsymbol{\beta}_{\boldsymbol{g}_s} \odot \boldsymbol{d}}{\|\boldsymbol{d}\|^2}$ are positive with greater amplitudes for e2, resulting in high positive values in the $\frac{\boldsymbol{\beta}_{\boldsymbol{g}_s} \odot \boldsymbol{d}}{\|\boldsymbol{d}\|^2}$ difference map. Consequently, summing up the $\frac{\boldsymbol{\beta}_{\boldsymbol{g}_s} \odot \boldsymbol{d}}{\|\boldsymbol{d}\|^2}$ difference map leads to a high $r(\Delta\boldsymbol{m}, \mathrm{GS})$ value. In contrast, for the Tx axis, $\frac{\boldsymbol{d}}{\|\boldsymbol{d}\|^2}$ shows high positive and negative values on the left and right edges, respectively, whereas $\boldsymbol{\beta}_{\boldsymbol{g}_s}$ shows high positive values across the cortex, including both the left and right edges. The resulting high positive and negative values observed in the $\frac{\boldsymbol{\beta}_{\boldsymbol{g}_s} \odot \boldsymbol{d}}{\|\boldsymbol{d}\|^2}$

difference map tend to cancel out, resulting in a lower $r(\Delta\boldsymbol{m}, \mathrm{GS})$ value. Together, these observations suggest that the GS bias in the Tz motion estimates is a result of $\boldsymbol{\beta_{g_s}}$ and $\boldsymbol{d}$ sharing a relatively similar top-bottom asymmetric spatial pattern.

In the Ty axis, as shown in Fig. S3, $\frac{\boldsymbol{d}}{\|\boldsymbol{d}\|^2}$ exhibits negative and positive values at the anterior and posterior edges of the brain, respectively, whereas $\boldsymbol{\beta_{g_s}}$ exhibits positive values across the cortex, including the posterior edge of the brain but exhibits relatively low values (approaching zero) along the anterior edge. As a result, the positive values in the $\frac{\boldsymbol{\beta_{g_s}} \odot \boldsymbol{d}}{\|\boldsymbol{d}\|^2}$ difference show relatively greater amplitudes as compared to the negative values, resulting in a high $r(\Delta\boldsymbol{m}, \mathrm{GS})$ value.

Taken together, the GS-induced bias in the Ty and Tz motion estimates relfect the asymmetries in $\boldsymbol{\beta_{g_s}}$ maps, which show higher values at the superior and posterior parts of the brain as compared to the inferior and anterior parts of the brain.

3.4. Effect of the bias on ROI-ROI FC via motion regression

In this section, we investigate how the presence of the GS-induced bias in the motion estimates affects the ROI-ROI FC by examining the differences in the ROI-ROI FC calculated after e2 and e1 motion regression. The e2-e1 differences in r-values and z-scores are denoted as Δr and Δz, respectively. Note that motion censoring was applied before motion regression. Fig. 4 shows Δr and Δz for all pairs of ROIs averaged over four groups of runs: (a) low motion and high aGS runs, (b) low motion and low aGS runs, (c) high motion and high aGS runs, and (d) high motion and low aGS runs. All four groups demonstrate negative Δr and Δz values for all pairs of ROIs, suggesting that the bias in the motion estimates can reduce FC estimates via motion regression. Comparing groups, we observed that the runs with low motion and high aGS exhibit the most negative Δr and Δz values (Δr ranging from -0.02 to -0.09 and Δz ranging from -0.63 to -1.41), while the runs with high motion and low aGS show Δr and Δz values close to zero (Δr ranging from -0.00 to -0.02 and Δz ranging from -0.05 to -0.33).

Furthermore, a one-way ANOVA on the mean Δz values calculated over ROI pairs showed that there is a significant ($p < 1 \times 10^{-6}$, $F_{3,598} = 40.53$) difference among groups. The results from the post-hoc t-tests indicate that the low motion and high aGS runs exhibit significantly ($p < 1 \times 10^{-4}$) more negative mean Δz values as compared to the other three groups, whereas the high motion and low aGS runs exhibit significantly ($p < 1 \times 10^{-6}$) less negative mean Δz values as compared to the other three groups. There is no significant ($p > 0.01$) difference between the group of low motion and low aGS runs and the group of high motion and high aGS runs. The distributions of the mean Δz values over ROI pairs for

the four groups can be found in Fig. S5.

Fig. S6 and S7 demonstrate that the observed effect of the bias is dominated by the motion estimates in the Ty and Tz axes. In Fig. S6, when including only the Ty and Tz motion regressors, the results are similar to those shown in Fig. 4. In contrast, when excluding the Ty and Tz motion regressors (Fig. S7), we observed minimal differences between the FC estimates obtained with e1 and e2 motion regression. Together, these results indicate that regressing out the motion estimates with GS-induced bias may lead to reductions in FC estimates, and there is a stronger effect for runs with higher aGS and lower head motion.

3.4.1. Effect of the bias on young vs. old group-level analysis

As shown in Fig. 5 (a) and (b), young subjects show significantly ($p < 1 \times 10^{-6}$) higher aGS and lower mean FD values as compared to the old subjects. Consequently, as shown in Fig. 5 (c), the young subjects show significantly ($p < 1 \times 10^{-6}$) more negative mean Δz values over ROI pairs as compared to the old subjects. The mean Δz values over runs and ROI pairs are -0.69 and -0.17 for the young and old subjects, respectively. Furthermore, Fig. 5 (d) and (e) visualize the mean Δr and Δz values over the young and old subjects for all ROI pairs. We observed that for all ROI pairs, the young subjects show more negative Δr and Δz values as compared to the old subjects. Since Δz and Δr reflect the effect of the bias when performing motion regression, these results suggest a greater impact of the bias on the young subjects as compared to the old subjects.

Moreover, we examined whether the bias affects the group-level analysis between the young and the old subjects. Fig. 6 (a) shows the differences in ROI-ROI FC between the young and old subjects calculated after motion censoring and e1 motion regression. We observed that the young subjects show significantly ($p < 1 \times 10^{-3}$) higher FC than the old subjects for all ROI pairs, except for the pair between IPS and LatPar. However, after e2 motion regression, as shown in Fig. 6 (b), the significant differences for five pairs of ROIs become insignificant ($p > 0.01$), including the pairs between (1) PCC and FEF, (2) PCC and IPS, (3) LatPar and FEF, (4) LatPar and MT+ and (5) FEF and IPS. Additionally, Fig. 6 (c) and (d) show that e2 motion regression reduces the FC differences between young and old for all pairs of ROIs as compared to e1 motion regression. Furthermore, as shown in Fig. S8 and S9, we verified that the observed effect is dominated by regressing out the Ty and Tz motion regressors. Together, these results demonstrate that motion regression with biased motion estimates can lead to underestimation of FC differences between the young and old subjects.

4. Discussion

In this study, we used a public resting-state MEfMRI dataset to examine whether global brain activity can lead to bias in rsfMRI motion estimates and to characterize the potential impact on rsFC estimates. By examining the correlation between the GS and the difference in the motion estimates from the first and second echoes, we found evidence for GS-related bias in the Tz and Ty motion estimates. We also demonstrated that the GS-induced bias can lead to underestimation of rsFC estimates when using motion regression, with low motion and high aGS runs exhibiting the greatest reductions in FC due to the bias and high motion and low aGS runs showing minimal reductions in FC. Finally, we showed that regression with biased motion estimates can reduce rsFC differences between groups of young and old subjects, due in part to different levels of aGS and head motion between the groups.

Extending prior studies that examined bias in task-based fMRI motion estimates, we identified BOLD-weighted bias in rsfMRI motion estimates and investigated its effect on rsFC. Moreover, utilizing multi-echo fMRI data, we proposed a novel method to detect the BOLD-weighted bias in real motion estimates over a large sample of runs with rigorous statistical tests. In contrast, in (Freire and Mangin, 2001; Freire et al., 2002), the existence of the bias in task-based fMRI is primarily illustrated using simulation with experimental data limited to one scan. Moreoever, to investigate the underlying cause of the observed bias, we proposed an empirical approximation to $r(\Delta \boldsymbol{m}, \mathrm{GS})$ and used this approximation to demonstrate how the presence of the GS-induced bias in the motion estimates may be attributed to the superior-inferior and posterior-anterior asymmetric spatial patterns in the GS beta coefficient map $\boldsymbol{\beta}_{\boldsymbol{g}_s}$.

While the interpretation of the GS is still controversial (reviewed in (Liu and Falahpour, 2020)), there is growing evidence suggesting that the GS is linked to vigilance (also known as arousal level) (Wong et al., 2013, 2016; Falahpour et al., 2016, 2018; Liu et al., 2018; Gu et al., 2021). For example, Falahpour et al. (2016) found that the GS is negatively correlated with the EEG vigilance. Furthermore, studies have shown that the vigilance templates, calculated as voxel-wise correlations between the EEG vigilance and the fMRI signal, can be used to estimate the EEG vigilance fluctuations during the fMRI scans (Chang et al., 2016; Falahpour et al., 2018; Goodale et al., 2021). To investigate whether the asymmetric spatial patterns in $\boldsymbol{\beta}_{\boldsymbol{g}_s}$ are associated with the vigilance, Fig. S10 compares $\boldsymbol{\beta}_{\boldsymbol{g}_s}$ from the example run shown in Fig. 3 to the eyes-open vigilance template estimated in (Falahpour et al., 2018) (both spatial maps were transferred to the MNI152 standard space). As shown in Fig. S10 (b), the estimated vigilance template

exhibits similar superior-inferior and posterior-anterior asymmetric spatial patterns to the example $\boldsymbol{\beta_{g_s}}$ map, resulting in a strong negative correlation ($r = -0.38$, $p < 1 \times 10^{-6}$) between $\boldsymbol{\beta_{g_s}}$ and the vigilance template. Hence, the asymmetric spatial patterns in $\boldsymbol{\beta_{g_s}}$ may be attributed to resting-state global brain activity linked to vigilance changes.

We also found that the posterior-anterior asymmetry pattern in $\boldsymbol{\beta_{g_s}}$ may be associated with the spatial intensity inhomogeneity in the fMRI data, a slow and smooth variation related to a combination of radio-frequency coil homogeneity, the pulse sequences used and the imaged object itself (Belaroussi et al., 2006). To illustrate the effect of the intensity inhomogeneity, Fig. S11 shows the reference images and estimated bias field maps from two low motion example runs, one with a high Ty $r(\Delta\boldsymbol{m}, \mathrm{GS})$ value of 0.87 (the example run shown in Fig. S3) and one with a low Ty $r(\Delta\boldsymbol{m}, \mathrm{GS})$ value of 0.07 (an example run has not shown before). For the example run with a strong $r(\Delta\boldsymbol{m}, \mathrm{GS})$ in the Ty axis shown in Fig. S11 (a), its reference image and estimated bias field map exhibit higher values at the posterior part of the brain and lower values at the anterior part of the brain. Whereas, for the run with $r(\Delta\boldsymbol{m}, \mathrm{GS})$ close to zero (shown in Fig. S11 (b)), its reference image and estimated bias field map show comparable values at the anterior and posterior parts of the brain.

While this work primarily focused on motion estimates from AFNI *3dvolreg*, we also performed a supplementary examination of the $r(\Delta\boldsymbol{m}, \mathrm{GS})$ values calculated with motion estimates from different algorithms, including FSL (Jenkinson and Smith, 2001; Jenkinson et al., 2002), ANTS (Avants et al., 2011, 2014) and SPM (Friston et al., 1995) and cost functions, including the least-squares (LS), normalized correlation (NC) and mutual information (MI) cost functions. (See sections S1.1 and S2.2 in the supplementary materials for details). In conclusion, both the algorithms and cost functions affect the level of the bias in the Ty and Tz axes, with the algorithms having a greater impact than the cost functions. Specifically, AFNI (LS) and SPM (LS) show a relatively greater level of the bias, FSL with different cost functions (LS, NC and MI) shows a moderate level of the bias, and ANTS (MI) shows the lowest level of the bias. Future work is needed to thoroughly examine how different algorithms and cost functions affect the level of the bias in the motion estimates.

In this study, we demonstrated that regression with biased motion estimates can reduce rsFC differences between the young and old subjects with the DMN and TPN ROIs. Importantly, we showed in Fig. 6 that the significant rsFC differences for five pairs of ROIs became insignificant ($p > 0.01$) due to regression with the biased motion estimates. Among these five pairs of ROIs, four of them are connections between DMN and TPN. These findings suggest that regression with biased motion estimates

may impede the detection of rsFC differences between the young and old groups. Because rsFC of the DMN plays a key role in understanding the aged brain (reviewed in (Ferreira and Busatto, 2013)), it can be important for future aging studies to minimize the effect of the bias on rsFC analyses. Based on our results, investigators can use motion estimates from the first echo data (if available) or consider excluding the Ty and Tz motion estimates from the motion regression. Moreover, our findings indicate that the biased motion estimates may lead to discrepancies in rsFC results via regression. Therefore, when comparing results from existing aging studies with different processing methodologies, the potential effect of the bias needs to be considered. Concerning this matter, future work that thoroughly examines the effect of the bias on the young vs. old rsFC analysis would be helpful.

Our findings revealed that the effect of the bias on the young vs. old rsFC analysis may be caused by different levels of aGS and head motion between the groups, with the old subjects showing a lower level of aGS and a higher level of head motion than the young subjects. It has been reported that old subjects tend to have greater head motion during rsfMRI scans (Saccà et al., 2021; Hausman et al., 2022), which reflects declined executive functioning with aging (Hausman et al., 2022). On the other hand, a direct comparison of aGS between young and old groups appears to be outside of prior studies. Nevertheless, previous studies have reported that old subjects show lower rsFC and BOLD variability (measured as the standard deviation of BOLD timeseries) in large-scale brain networks, including the DMN, compared to young subjects (Ferreira and Busatto, 2013; Grady and Garrett, 2018; Nomi et al., 2017; Kumral et al., 2020), supporting the observed lower aGS in the old subjects.

In conclusion, we found that resting-state global brain activity can lead to bias in Ty and Tz motion estimates obtained with a widely used motion correction algorithm. Furthermore, the bias in the motion estimates can lead to reductions in the ROI-ROI rsFC obtained after motion regression, with an increasing level of effect for runs showing higher aGS and lower head motion. Moreover, our results show that the bias can reduce group-level FC differences between young and old subjects. To minimize the effect of the bias, investigators can use motion estimates from the first echo data (if available) or consider excluding the Ty and Tz motion estimates from the motion regression. Future work is needed to investigate the dependence of the bias on the registration algorithm and scan parameters. In addition, future work focused on developing registration algorithms with minimal bias would be helpful.

5. Acknowledgements

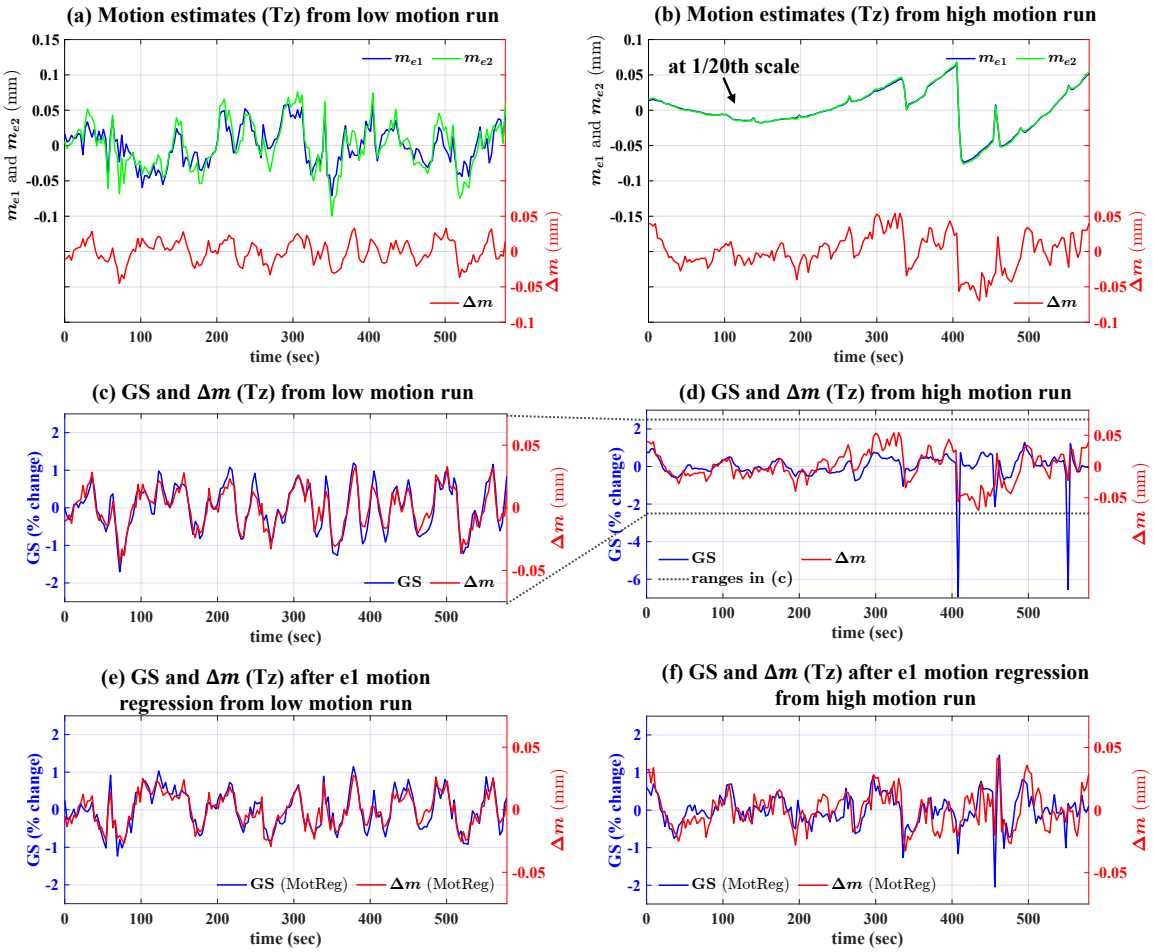

Figure 1: Motion estimates in the Tz axis, including $\boldsymbol{m}_{e1}$ (blue), $\boldsymbol{m}_{e2}$ (green) and $\Delta\boldsymbol{m}$ (red) from (a) low and (b) high motion runs. Panels (c) and (d) show the GS (blue) and $\Delta\boldsymbol{m}$ (red) from the low and high motion runs, respectively. Panels (e) and (f) show the GS (blue) and $\Delta\boldsymbol{m}$ (red) after motion regression (MotReg) from the low and high motion runs, respectively.

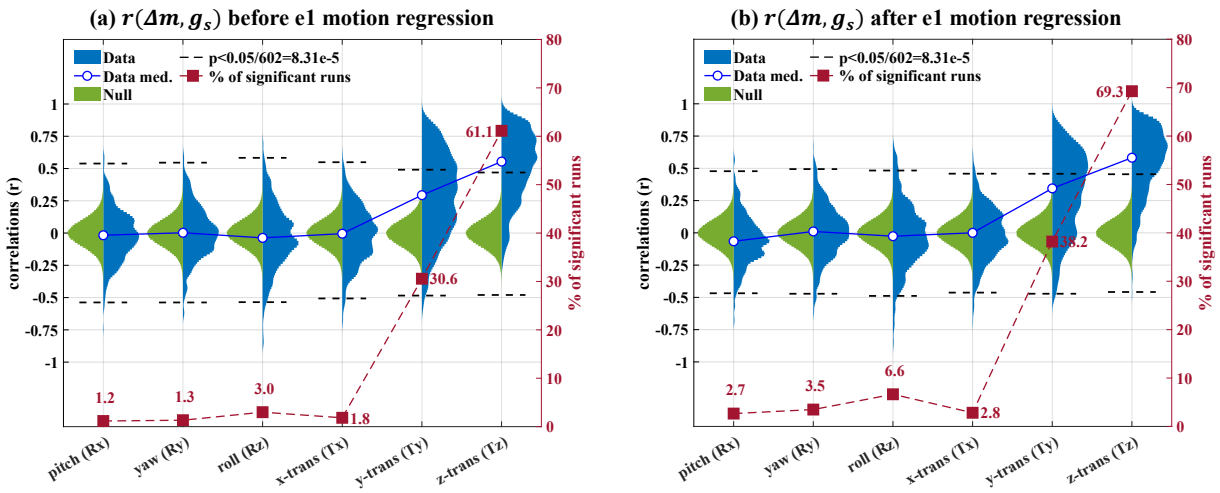

Figure 2: Two-sided violin plots showing the distributions of $r(\Delta \boldsymbol{m}, \mathrm{GS})$ values (blue) and the empirical null distributions (green) for all six motion axes (a) before and (b) after e1 motion regression. The blue solid lines and circles represent the median values for each data distribution. For each motion axis, a run-wise p-value threshold of 0.05 was used and the p-value threshold was divided by the number of runs to correct for multiple comparisons. The black dashed lines show $r(\Delta \boldsymbol{m}, \mathrm{GS})$ values that correspond to the p-value thresholds (two-sided) assessed from the empirical null distributions. The dark red dashed lines and square markers represent the percent of the runs with significant $r(\Delta \boldsymbol{m}, \mathrm{GS})$ values.

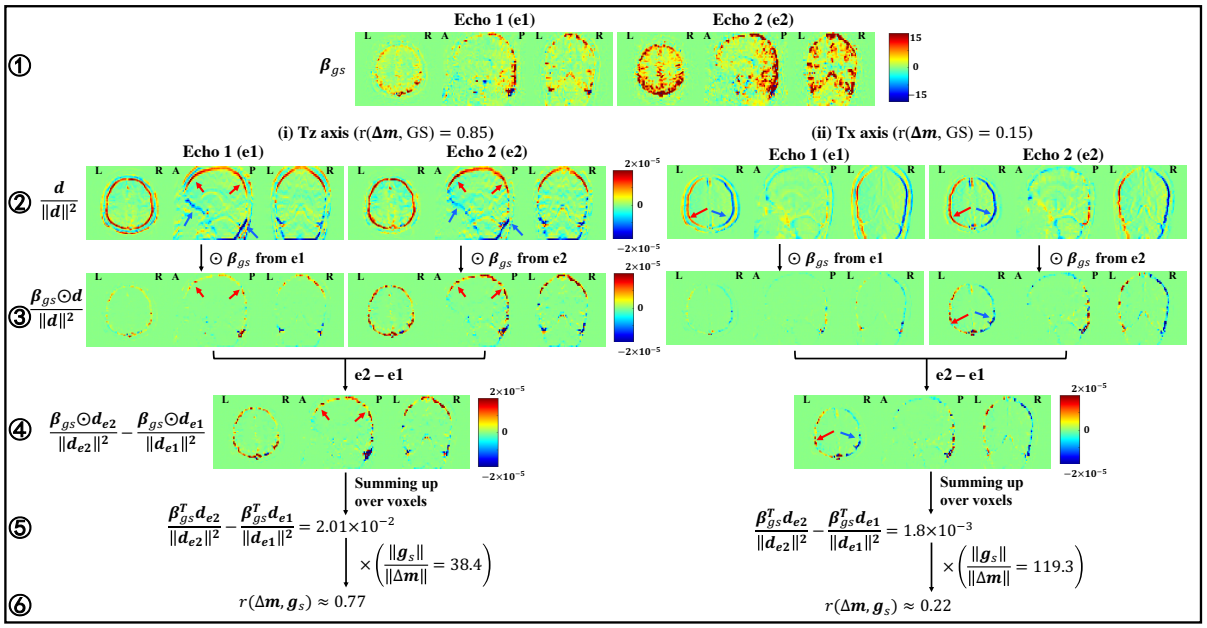

Figure 3: Visualization of the spatial maps underlying $r(\Delta\boldsymbol{m}, \mathrm{GS})$ in the Tz and Tx axes from an example run. For each map, three representative slices (one axial, one sagittal and one coronal) are plotted. From top to bottom, rows 1 through 3 show the $\boldsymbol{\beta_{g_s}}$, $\frac{\boldsymbol{d}}{\|\boldsymbol{d}\|^2}$, and $\frac{\boldsymbol{\beta_{g_s}} \odot \boldsymbol{d}}{\|\boldsymbol{d}\|^2}$ maps from e1 and e2, where $\odot$ represents element-wise multiplication. Row 4 shows $\frac{\boldsymbol{\beta_{g_s}} \odot \boldsymbol{d}}{\|\boldsymbol{d}\|^2}$ difference (e2-e1) maps. From left to right in rows 2 and 3, the first and second columns show the e1 and e2 maps in the Tz axis, and the third and fourth columns show the e1 and e2 maps in the Tx axis. The red and blue arrows point to brain regions showing high positive and negative values in the maps, respectively.

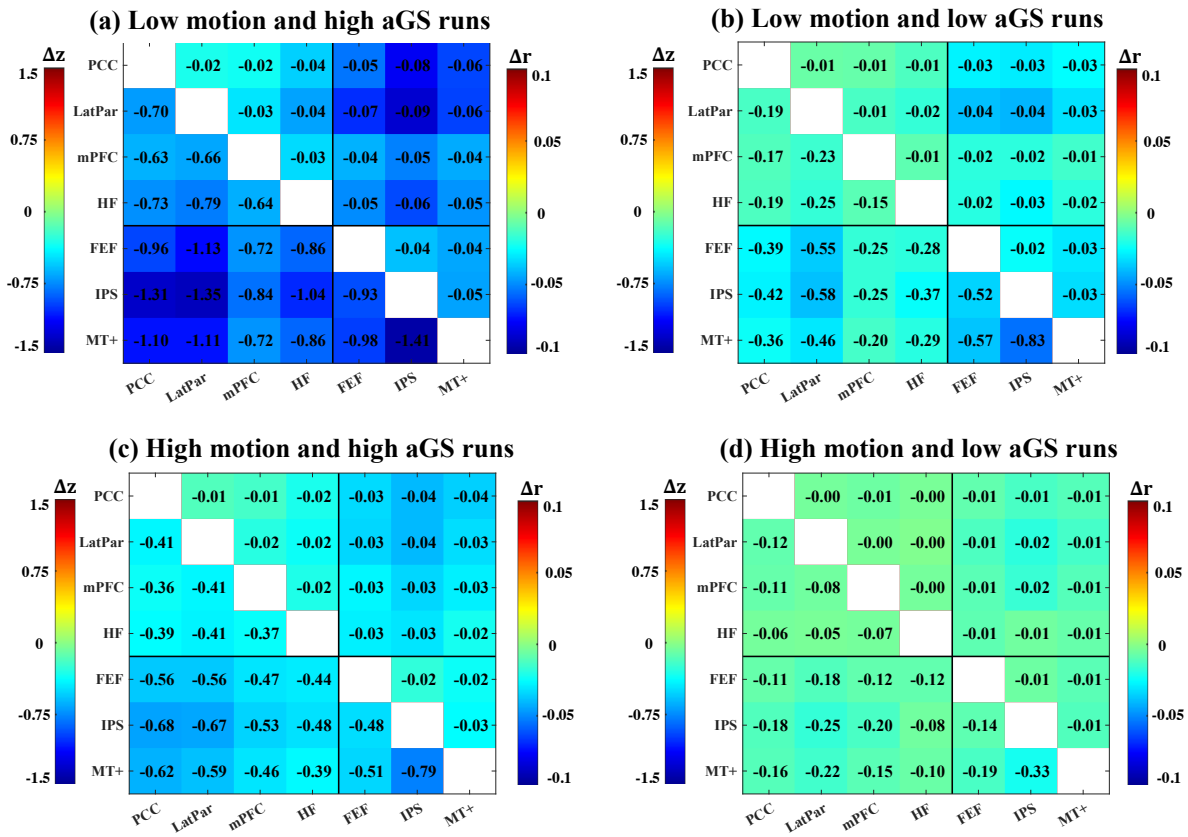

Figure 4: Differences (e2-e1) in ROI-ROI FC calculated after e2 and e1 motion regression. The differences were averaged across runs within each of four groups: (a) low motion and high aGS runs, (b) low motion and low aGS runs, (c) high motion and high aGS runs and (d) high motion and low aGS runs. Each subplot is divided into an upper right triangle showing the averaged differences in r-values and a lower left triangle showing the the averaged differences in z-scores.

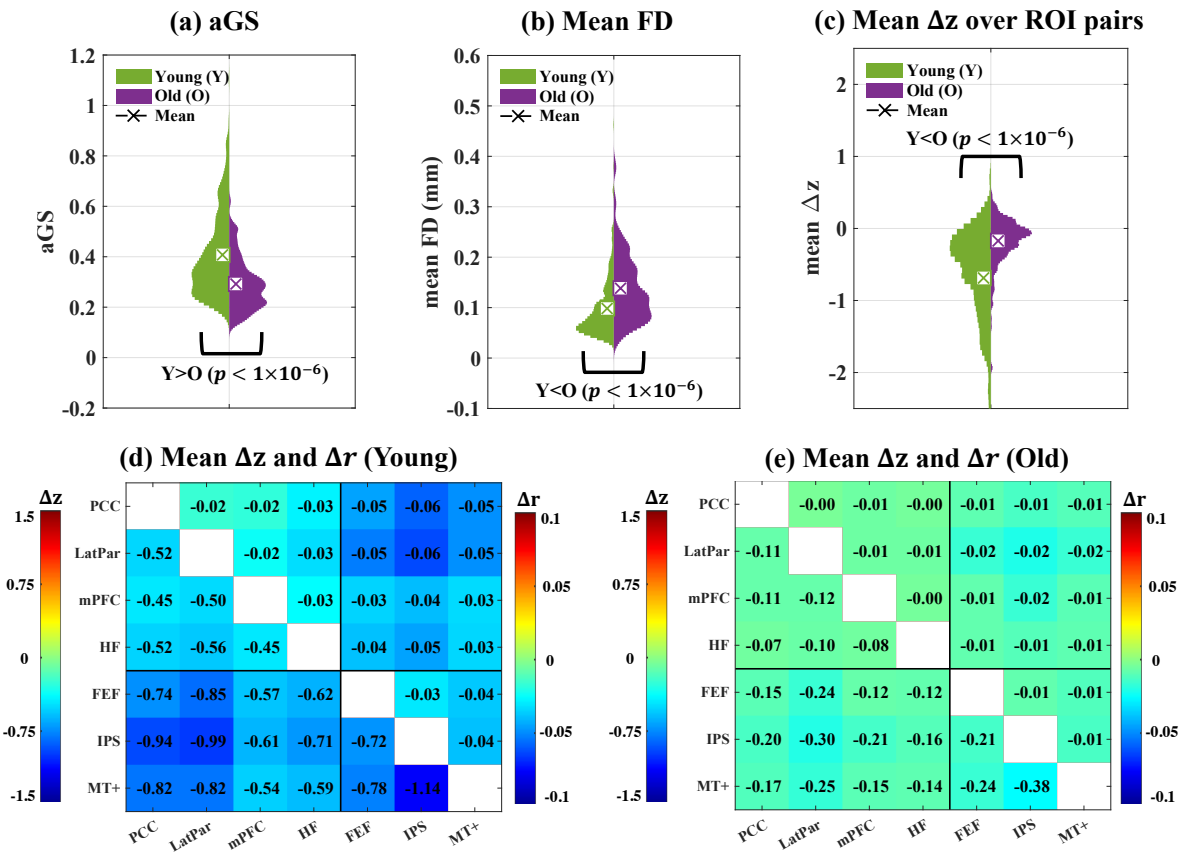

Figure 5: (a-c) Two-sided violin plots showing the distributions of (a) aGS, (b) mean FD and (c) mean Δz (e2-e1) over ROI pairs for the young (green) and old (purple) subjects. Two-sided permutation tests were calculated to assess the significance thresholds for the differences between the young and old subjects. Young subjects show significantly ($p < 1 \times 10^{-6}$) larger aGS, smaller mean FD and more negative mean Δz as compared to the old subjects. Panels (d-e) show the mean Δz and Δr over (d) young and (e) old subjects for all ROI pairs. Each subplot is divided into an upper right triangle showing the averaged differences in r-values and a lower left triangle showing the the averaged differences in z-scores.

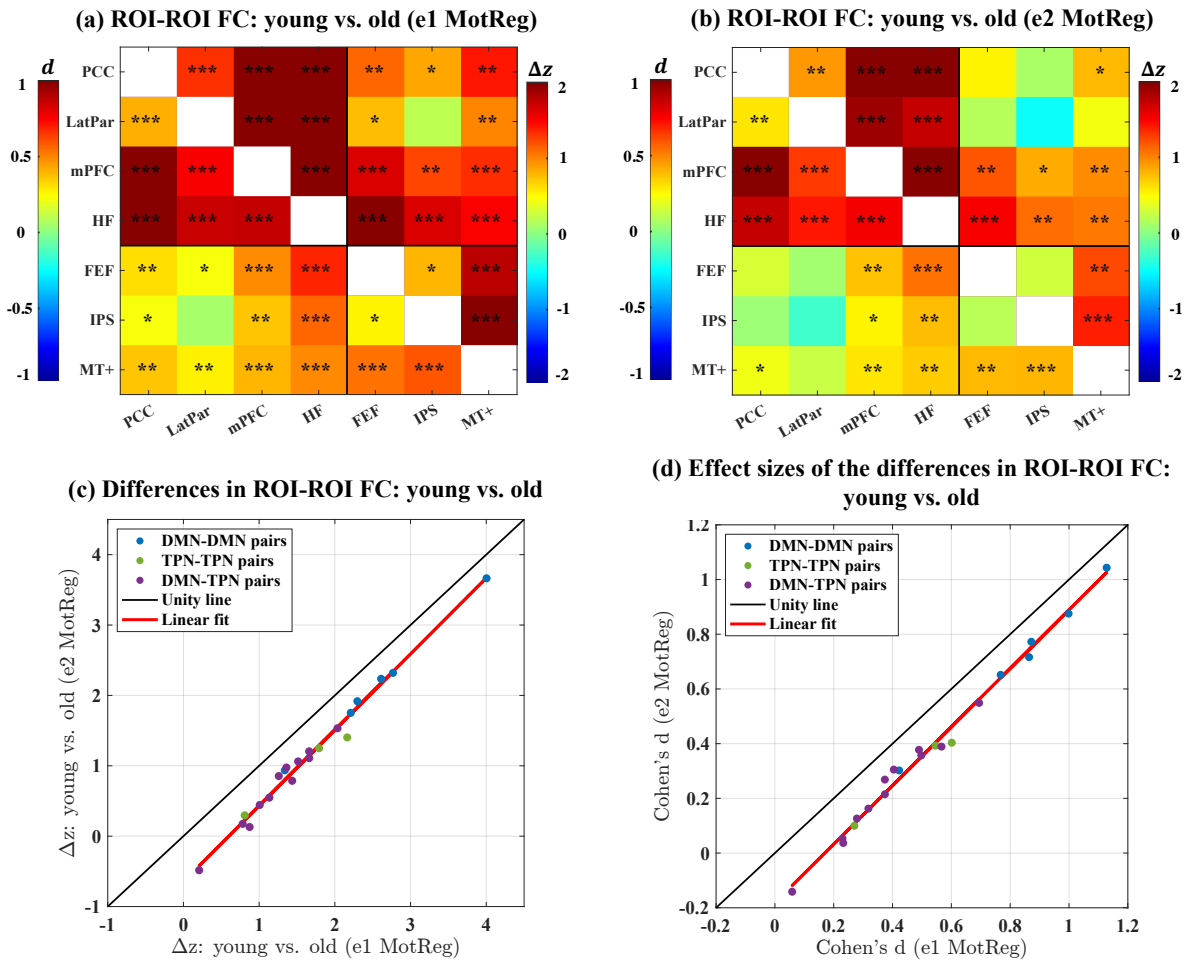

Figure 6: (a-b) ROI-ROI FC differences (young-old) between young and old subjects calculated after (a) e1 and (b) e2 motion regression. Each subplot is divided into an upper right triangle showing the averaged differences in z-scores between young and old subjects and a lower left triangle showing the effect size of the differences. The black asterisks indicate the statistical significance of the differences assessed by permutation tests (*: $p < 0.01$, **: $p < 1 \times 10^{-3}$, ***: $p < 1 \times 10^{-6}$). A positive value (red color) indicates that the young subjects show higher connectivity as compared to the old subjects. (c) Scatter plot comparing the differences in ROI-ROI FC between the young and the old subjects calculated after e1 and e2 motion regression for all pairs of ROIs. (d) Scatter plot comparing the effect sizes of the differences in ROI-ROI FC between the young and the old subjects calculated after e1 and e2 motion regression for all pairs of ROIs. e1 MotReg: e1 motion regression; e2 MotReg: e2 motion regression.

Appendix A. Motion estimation in AFNI *3dvolreg*

In this section, we review the theory and implementation of AFNI *3dvolreg*. Let $\boldsymbol{Y} = [\boldsymbol{y}_1, \boldsymbol{y}_2, ..., \boldsymbol{y}_K] \in \mathbb{R}^{N\times K}$ be the functional data, where N is the number of voxels, K is the number of volumes and $\boldsymbol{y}_k \in \mathbb{R}^{N\times 1}$ is the kth column of $\boldsymbol{Y}$, i.e. the kth volume of the data with $k = 1, 2, ..., K$. Let $\boldsymbol{y}_r \in \mathbb{R}^{N\times 1}$ be the reference image used in the registration. To align $\boldsymbol{y}_k$ to $\boldsymbol{y}_r$, the algorithm first estimates the motion parameters $\boldsymbol{a}_k \in \mathbb{R}^{6\times 1}$ (consisting of 3 rotational and 3 translational motion parameters) by iteratively minimizing the weighted least square cost function:

$$\boldsymbol{a}_k = \arg\min_{\boldsymbol{a}} ||\boldsymbol{W}^{\frac{1}{2}}(\boldsymbol{y}_k - T(\boldsymbol{y}_r, \boldsymbol{a}))||_2^2 \tag{A.1}$$

where $\boldsymbol{W}$ is a diagonal weight matrix and $T : \mathbb{R}^{N\times 1} \to \mathbb{R}^{N\times 1}$ is the function that performs rigid body transformation. Because we disabled the weights, we have $\boldsymbol{W} = \boldsymbol{I}$, where $\boldsymbol{I}$ is the identity matrix. After obtaining $\boldsymbol{a}_k$, the algorithm then transforms $\boldsymbol{y}_k$ with $-\boldsymbol{a}_k$, which can be written as $T(\boldsymbol{y}_k, -\boldsymbol{a}_k)$, to register $\boldsymbol{y}_k$ to $\boldsymbol{y}_r$. To solve the minimization problem in Eq. A.1, the algorithm linearizes the rigid body transformation with a first-order Taylor approximation, which can be written as

$$T(\boldsymbol{y}_r, \boldsymbol{a}) \approx \boldsymbol{y}_r + \sum_{j}^{6} a_j \frac{\partial T(\boldsymbol{y}_r, \boldsymbol{a})}{\partial a_j} \tag{A.2}$$

where a_j is the jth element of $\boldsymbol{a}$. Furthermore, the partial derivatives in Eq. A.2 are approximated with finite differences:

$$\boldsymbol{d}_j \triangleq \frac{\partial T(\boldsymbol{y}_r, \boldsymbol{a})}{\partial a_i} \approx \frac{T(\boldsymbol{y}_r, \epsilon \boldsymbol{s}_j) - T(\boldsymbol{y}_r, -\epsilon \boldsymbol{s}_j)}{2\epsilon}, \quad j = 1, 2, ..., 6 \tag{A.3}$$

where ϵ is a scalar with small magnitude and $\boldsymbol{s}_j$ is a 6×1 vector whose jth element is one while the other elements are zeros. Here, we use $\boldsymbol{d}_j \in \mathbb{R}^{N\times 1}$ to represent the partial derivative with respect to (w.r.t.) a_j and refer to it as the spatial derivative image w.r.t. the jth motion axis. The linearization of the transformation can then be written as

$$T(\boldsymbol{y}_r, \boldsymbol{a}) \approx \boldsymbol{y}_r + \boldsymbol{D}\boldsymbol{a} \tag{A.4}$$

where $\boldsymbol{D} = [\boldsymbol{d}_1, \boldsymbol{d}_2, ..., \boldsymbol{d}_6] \in \mathbb{R}^{N\times 6}$. With the above linearization and $\boldsymbol{W} = \boldsymbol{I}$, the minimization problem in Eq. A.1 can be written as

$$\boldsymbol{a}_k = \arg\min_{\boldsymbol{a}} ||\boldsymbol{y}_k - \boldsymbol{y}_r - \boldsymbol{D}\boldsymbol{a}||_2^2 \tag{A.5}$$

In AFNI *3dvolreg*, the motion parameters are estimated by iteratively minimizing the cost function in Eq. A.5. Let $\boldsymbol{a}_{k,n}$ denote the motion parameters estimated at the nth iteration,

$$\boldsymbol{a}_{k,n} = (\boldsymbol{D}^T\boldsymbol{D})^{-1}\boldsymbol{D}^T(\boldsymbol{y}_{k,n} - \boldsymbol{y}_r) \quad n = 1, 2, ..., N_k \tag{A.6}$$

where N_k is the total number of iterations for the kth volume and $\boldsymbol{y}_{k,n}$ can be written as

$$\boldsymbol{y}_{k,n} = \begin{cases} \boldsymbol{y}_k, & n = 1 \\ T(\boldsymbol{y}_{k,n-1}, -\boldsymbol{a}_{k,n-1}), & n = 2, 3, ...N_k \end{cases} \tag{A.7}$$

The algorithm stops the iterative process if $\boldsymbol{a}_{k,n}$ is smaller than some fixed thresholds (for the used dataset, the translational and rotational thresholds are 0.03 mm and 0.02 degree, respectively) or N_k exceeds the maximum number of iterations, denoted as N_{max}. The algorithm uses this iterative process to deal with the approximation error in the linearization of the rigid transformation described in Eq.A.4. In practice, for most volumes, the iterative process stops at the second iteration, suggesting that the parameters estimated in the second iteration are smaller than the thresholds and Eq.A.4 is a valid approximation. After the iterative estimation process stops, the motion parameters of the kth volume are calculated by summing the estimated parameters over all iterations:

$$\boldsymbol{a}_k = \sum_{n=1}^{N_k} \boldsymbol{a}_{k,n} \tag{A.8}$$

Stacking the motion parameters over volumes yields

$$\boldsymbol{M} = [\boldsymbol{a}_1^T; \boldsymbol{a}_2^T; ...; \boldsymbol{a}_K^T] \tag{A.9}$$

Here, the jth column of $\boldsymbol{M}$ represents the time series of the motion parameters of the jth motion axis (denoted as $\boldsymbol{m}_j$). Furthermore, in order to explicitly show the relation between $\boldsymbol{M}$ and the functional data $\boldsymbol{Y}$, we define $\boldsymbol{y}_{k,n} = \boldsymbol{y}_r$ for $N_k < n \leq N_{max}$ so that $\boldsymbol{a}_{k,n} = \boldsymbol{0}$ for $N_k < n \leq N_{max}$. Therefore, the motion parameters can be written as

$$\begin{aligned} \boldsymbol{M} &= [\sum_{n=1}^{N_{max}} \boldsymbol{a}_{1,n}^T; \sum_{n=1}^{N_{max}} \boldsymbol{a}_{2,n}; ...; \sum_{n=1}^{N_{max}} \boldsymbol{a}_{K,n}^T] \\ &= \sum_{n=1}^{N_{max}} [(\boldsymbol{y}_{1,n} - \boldsymbol{y}_r)^T; (\boldsymbol{y}_{2,n} - \boldsymbol{y}_r)^T; ...; (\boldsymbol{y}_{K,n} - \boldsymbol{y}_r)^T]\boldsymbol{D}(\boldsymbol{D}^T\boldsymbol{D})^{-1} \\ &= \sum_{n=1}^{N_{max}} (\boldsymbol{Y}_n^T - \boldsymbol{1}_K\boldsymbol{y}_r^T)\boldsymbol{D}(\boldsymbol{D}^T\boldsymbol{D})^{-1} \end{aligned} \tag{A.10}$$

where $\boldsymbol{Y}_n = [\boldsymbol{y}_{1,n}, \boldsymbol{y}_{2,n}, ..., \boldsymbol{y}_{K,n}]$ and $\mathbf{1}_K$ is a K by 1 all-one vector. Here, $(\boldsymbol{Y}_n^T - \mathbf{1}_K \boldsymbol{y}_r^T)\boldsymbol{D}(\boldsymbol{D}^T\boldsymbol{D})^{-1}$ represents the parameters estimated at the nth iteration.

In practice, the algorithm directly estimates and outputs the transformation parameters used to align $\boldsymbol{y}_k$ to $\boldsymbol{y}_r$ (i.e., $-\boldsymbol{a}_k$) by using $-\boldsymbol{D}$. Therefore, in this work, the transformation parameters generated by AFNI *3dvolreg* were multiplied by -1 to represent the motion parameters $\boldsymbol{a}_k$.

Appendix B. Empirical approximations to the motion estimates

To explore the key terms underlying $r(\Delta\boldsymbol{m}, \mathrm{GS})$, we derived the following empirical approximations to the motion estimates:

$$\begin{aligned}
\boldsymbol{M} &= \underbrace{(\boldsymbol{Y}^T - \mathbf{1}_K \boldsymbol{y}_r^T)\boldsymbol{D}(\boldsymbol{D}^T\boldsymbol{D})^{-1}}_{\text{1st iteration}} + \underbrace{\sum_{n=2}^{N_{max}} (\boldsymbol{Y}_n^T - \mathbf{1}_K \boldsymbol{y}_r^T)\boldsymbol{D}(\boldsymbol{D}^T\boldsymbol{D})^{-1}}_{\text{other iterations}} \\
&\approx \boldsymbol{M}_{A1} = (\boldsymbol{Y}^T - \mathbf{1}_K \boldsymbol{y}_r^T)\boldsymbol{D}(\boldsymbol{D}^T\boldsymbol{D})^{-1} && \text{(Approx. 1)} \\
&\approx \boldsymbol{M}_{A2} = \boldsymbol{Y}^T\boldsymbol{D}(\boldsymbol{D}^T\boldsymbol{D})^{-1} && \text{(Approx. 2)} \\
&\approx \boldsymbol{M}_{A3} = \boldsymbol{Y}^T\boldsymbol{D}(diag(diag(\boldsymbol{D}^T\boldsymbol{D})))^{-1} && \text{(Approx. 3)}
\end{aligned} \tag{B.1}$$

where $\mathbf{1}_K \in \mathbb{R}^{K\times 1}$ is an all-one vector and *diag()* denotes the Matlab function `diag()`. The first approximation of the motion estimates, denoted as $\boldsymbol{M}_{A1}$, are the motion parameters estimated at the first iteration. This approximation is valid when Eq.A.4 shows minimal approximation error. Then, because the reference image is almost orthogonal to the derivative images (i.e., $\boldsymbol{D}^T\boldsymbol{y}_r \approx \mathbf{0}$), we made the second approximation, denoted as $\boldsymbol{M}_{A2}$, as the motion parameters estimated without subtracting the reference image from the functional data. The third approximation of the motion estimates, denoted as $\boldsymbol{M}_{A3}$, are the motion parameters estimated after zeroing out the off-diagonal terms in $\boldsymbol{D}^T\boldsymbol{D}$, reflecting the fact that the covariance between the derivative images in different axes is relatively small compared to the variance of the derivative images. To evaluate the approximations, the temporal correlations between $\boldsymbol{M}$ and the approximated motion estimates were calculated for each motion axis. As shown in Fig. S13, $\boldsymbol{M}$ is highly correlated with $\boldsymbol{M}_{A1}$ (mean $r = 0.99$), $\boldsymbol{M}_{A2}$ (mean $r = 0.99$), and $\boldsymbol{M}_{A3}$ (mean $r = 0.91$)). Fig. S14 displays the motion estimates before and after the approximations in the Tz and Ty axes from three example runs.

With the third approximation, the motion estimates of one motion axis, denoted as $\boldsymbol{m}_{A3} \in \mathbb{R}^{K\times 1}$

can be written as

$$\boldsymbol{m}_{A3} = \frac{\boldsymbol{Y}^T \boldsymbol{d}}{\|\boldsymbol{d}\|^2} \tag{B.2}$$

where $\boldsymbol{d} \in \mathbb{R}^{N\times 1}$ is the spatial derivative image w.r.t. that motion axis.

Appendix C. The approximation to $r(\Delta \boldsymbol{m}, \mathrm{GS})$

To interpret $r(\Delta \boldsymbol{m}, \mathrm{GS})$, we derived a mathematical approximation that reveals the key factors. We begin with the expression

$$r(\boldsymbol{g}_s, \Delta \boldsymbol{m}) = \frac{\boldsymbol{g}_s^T \Delta \boldsymbol{m}}{\|\Delta \boldsymbol{m}\| \|\boldsymbol{g}_s\|} = \frac{\boldsymbol{g}_s^T (\boldsymbol{m}_{e2} - \boldsymbol{m}_{e1})}{\|\Delta \boldsymbol{m}\| \|\boldsymbol{g}_s\|} \tag{C.1}$$

where $\boldsymbol{g}_s \in \mathbb{R}^{K\times 1}$, $\Delta \boldsymbol{m} = \boldsymbol{m}_{e2} - \boldsymbol{m}_{e1} \in \mathbb{R}^{K\times 1}$ represent the GS and the difference between the e2 and e1 motion estimates, respectively, and $\boldsymbol{m}_{ei} \in \mathbb{R}^{K\times 1}$ represents the motion estimates from the ith echo. Then, using the approximation described in Eq.B.2, we can write

$$\begin{aligned} r(\Delta \boldsymbol{m}, \mathrm{GS}) &= \frac{\boldsymbol{g}_s^T (\boldsymbol{m}_{e2} - \boldsymbol{m}_{e1})}{\|\Delta \boldsymbol{m}\| \|\boldsymbol{g}_s\|} \\ &\approx \frac{\boldsymbol{g}_s^T \left(\frac{\boldsymbol{Y}_{e2}^T \boldsymbol{d}_{e2}}{\|\boldsymbol{d}_{e2}\|^2} - \frac{\boldsymbol{Y}_{e1}^T \boldsymbol{d}_{e1}}{\|\boldsymbol{d}_{e1}\|^2} \right)}{\|\Delta \boldsymbol{m}\| \|\boldsymbol{g}_s\|} \\ &= \frac{\|\boldsymbol{g}_s\|}{\|\Delta \boldsymbol{m}\|} \left(\frac{\boldsymbol{g}_s^T \boldsymbol{Y}_{e2}^T \boldsymbol{d}_{e2}}{\|\boldsymbol{g}_s\|^2 \|\boldsymbol{d}_{e2}\|^2} - \frac{\boldsymbol{g}_s^T \boldsymbol{Y}_{e1}^T \boldsymbol{d}_{e1}}{\|\boldsymbol{g}_s\|^2 \|\boldsymbol{d}_{e1}\|^2} \right) \\ &= \frac{\|\boldsymbol{g}_s\|}{\|\Delta \boldsymbol{m}\|} \left(\frac{\boldsymbol{\beta}_{\boldsymbol{g}_s, e2}^T \boldsymbol{d}_{e2}}{\|\boldsymbol{d}_{e2}\|^2} - \frac{\boldsymbol{\beta}_{\boldsymbol{g}_s, e1}^T \boldsymbol{d}_{e1}}{\|\boldsymbol{d}_{e1}\|^2} \right) \end{aligned} \tag{C.2}$$

where $\boldsymbol{\beta}_{\boldsymbol{g}_s, ei} = \frac{\boldsymbol{Y}_{ei}^T \boldsymbol{g}_s}{\|\boldsymbol{g}_s\|^2}$ is the GS beta coefficient map calculated from the linear fit of the GS to the unregistered functional data of the ith echo.

References

Avants, B.B., Tustison, N.J., Song, G., Cook, P.A., Klein, A., Gee, J.C., 2011. A reproducible evaluation of ANTs similarity metric performance in brain image registration. NeuroImage 54, 2033–2044. doi:10.1016/j.neuroimage.2010.09.025.

Avants, B.B., Tustison, N.J., Stauffer, M., Song, G., Wu, B., Gee, J.C., 2014. The Insight ToolKit image registration framework. Frontiers in Neuroinformatics 8, 44. doi:10.3389/fninf.2014.00044.

Belaroussi, B., Milles, J., Carme, S., Zhu, Y.M., Benoit-Cattin, H., 2006. Intensity non-uniformity correction in MRI: Existing methods and their validation. Medical Image Analysis 10, 234–246. doi:10.1016/j.media.2005.09.004.

Bright, M.G., Murphy, K., 2013. Removing motion and physiological artifacts from intrinsic BOLD fluctuations using short echo data. NeuroImage 64, 526–537. doi:10.1016/j.neuroimage.2012.09.043.

Buur, P.F., Poser, B.A., Norris, D.G., 2009. A dual echo approach to removing motion artefacts in fMRI time series. NMR in Biomedicine 22, 551–560. doi:10.1002/nbm.1371.

Chang, C., Leopold, D.A., Schölvinck, M.L., Mandelkow, H., Picchioni, D., Liu, X., Ye, F.Q., Turchi, J.N., Duyn, J.H., 2016. Tracking brain arousal fluctuations with fMRI. Proceedings of the National Academy of Sciences 113, 4518–4523. doi:10.1073/pnas.1520613113.

Cox, R.W., 1996. AFNI: Software for Analysis and Visualization of Functional Magnetic Resonance Neuroimages. Computers and Biomedical Research 29, 162–173. doi:10.1006/cbmr.1996.0014.

Cox, R.W., Jesmanowicz, A., 1999. Real-time 3D image registration for functional MRI. Magnetic Resonance in Medicine 42, 1014–1018. doi:10.1002/(sici)1522-2594(199912)42:6<1014::aid-mrm4>3.0.co;2-f.

Dijk, K.R.A.V., Hedden, T., Venkataraman, A., Evans, K.C., Lazar, S.W., Buckner, R.L., 2010. Intrinsic Functional Connectivity As a Tool For Human Connectomics: Theory, Properties, and Optimization. Journal of Neurophysiology 103, 297–321. doi:10.1152/jn.00783.2009.

Dijk, K.R.V., Sabuncu, M.R., Buckner, R.L., 2012. The influence of head motion on intrinsic functional connectivity MRI. NeuroImage 59, 431–438. doi:10.1016/j.neuroimage.2011.07.044.

Falahpour, M., Chang, C., Wong, C.W., Liu, T.T., 2018. Template-based prediction of vigilance fluctuations in resting-state fMRI. NeuroImage 174, 317–327. doi:10.1016/j.neuroimage.2018.03.012.

Falahpour, M., Wong, C.W., Liu, T.T., 2016. The resting state fMRI global signal is negatively correlated with time-varying EEG vigilance, in: Proceedings of the 24th Annual Meeting of the ISMRM, p. 641.

Ferreira, L.K., Busatto, G.F., 2013. Resting-state functional connectivity in normal brain aging. Neuroscience & Biobehavioral Reviews 37, 384–400. doi:10.1016/j.neubiorev.2013.01.017.

Freire, L., Mangin, J.F., 2001. Motion Correction Algorithms May Create Spurious Brain Activations in the Absence of Subject Motion. NeuroImage 14, 709–722. doi:10.1006/nimg.2001.0869.

Freire, L., Roche, A., Mangin, J.F., 2002. What is the Best Similarity Measure for Motion Correction in fMRI Time Series? IEEE Transactions on Medical Imaging 21, 470. doi:10.1109/tmi.2002.1009383.

Friston, K.J., Ashburner, J., Frith, C.D., Poline, J., Heather, J.D., Frackowiak, R.S.J., 1995. Spatial registration and normalization of images. Human Brain Mapping 3, 165–189. doi:10.1002/hbm.460030303.

Friston, K.J., Williams, S., Howard, R., Frackowiak, R.S.J., Turner, R., 1996. Movement-Related effects in fMRI time-series. Magnetic Resonance in Medicine 35, 346–355. doi:10.1002/mrm.1910350312.

Goodale, S.E., Ahmed, N., Zhao, C., Zwart, J.A.d., Özbay, P.S., Picchioni, D., Duyn, J., Englot, D.J., Morgan, V.L., Chang, C., 2021. fMRI-based detection of alertness predicts behavioral response variability. eLife 10, e62376. doi:10.7554/elife.62376.

Grady, C.L., Garrett, D.D., 2018. Brain signal variability is modulated as a function of internal and external demand in younger and older adults. NeuroImage 169, 510–523. doi:10.1016/j.neuroimage.2017.12.031.

Gu, Y., Sainburg, L.E., Kuang, S., Han, F., Williams, J.W., Liu, Y., Zhang, N., Zhang, X., Leopold, D.A., Liu, X., 2021. Brain Activity Fluctuations Propagate as Waves Traversing the Cortical Hierarchy. Cerebral Cortex 31, bhab064–. doi:10.1093/cercor/bhab064.

Hausman, H.K., Hardcastle, C., Kraft, J.N., Evangelista, N.D., Boutzoukas, E.M., O'Shea, A., Albizu, A., Langer, K., Etten, E.J.V., Bharadwaj, P.K., Song, H., Smith, S.G., Porges, E., Hishaw, G.A.,

Wu, S., DeKosky, S., Alexander, G.E., Marsiske, M., Cohen, R., Woods, A.J., 2022. The association between head motion during functional magnetic resonance imaging and executive functioning in older adults. Neuroimage: Reports 2, 100085. doi:10.1016/j.ynirp.2022.100085.

Jenkinson, M., Bannister, P., Brady, M., Smith, S., 2002. Improved Optimization for the Robust and Accurate Linear Registration and Motion Correction of Brain Images. NeuroImage 17, 825–841. doi:10.1006/nimg.2002.1132.

Jenkinson, M., Smith, S., 2001. A global optimisation method for robust affine registration of brain images. Medical Image Analysis 5, 143–156. doi:10.1016/s1361-8415(01)00036-6.

Kumral, D., *c*Sansal, F., Cesnaite, E., Mahjoory, K., Al, E., Gaebler, M., Nikulin, V., Villringer, A., 2020. BOLD and EEG signal variability at rest differently relate to aging in the human brain. NeuroImage 207, 116373. doi:10.1016/j.neuroimage.2019.116373.

Kundu, P., Inati, S.J., Evans, J.W., Luh, W.M., Bandettini, P.A., 2012. Differentiating BOLD and non-BOLD signals in fMRI time series using multi-echo EPI. NeuroImage 60, 1759–1770. doi:10.1016/j.neuroimage.2011.12.028.

Kundu, P., Voon, V., Balchandani, P., Lombardo, M.V., Poser, B.A., Bandettini, P.A., 2017. Multi-echo fMRI: A review of applications in fMRI denoising and analysis of BOLD signals. NeuroImage 154, 59–80. doi:10.1016/j.neuroimage.2017.03.033.

Liu, T.T., Falahpour, M., 2020. Vigilance Effects in Resting-State fMRI. Frontiers in Neuroscience 14, 321. doi:10.3389/fnins.2020.00321.

Liu, X., Zwart, J.A.d., Schölvinck, M.L., Chang, C., Ye, F.Q., Leopold, D.A., Duyn, J.H., 2018. Subcortical evidence for a contribution of arousal to fMRI studies of brain activity. Nature Communications 9, 395. doi:10.1038/s41467-017-02815-3.

Nomi, J.S., Bolt, T.S., Ezie, C.C., Uddin, L.Q., Heller, A.S., 2017. Moment-to-Moment BOLD Signal Variability Reflects Regional Changes in Neural Flexibility across the Lifespan. The Journal of Neuroscience 37, 5539–5548. doi:10.1523/jneurosci.3408-16.2017.

Power, J.D., Barnes, K.A., Snyder, A.Z., Schlaggar, B.L., Petersen, S.E., 2012. Spurious but systematic correlations in functional connectivity MRI networks arise from subject motion. NeuroImage 59, 2142–2154. doi:10.1016/j.neuroimage.2011.10.018.

Power, J.D., Mitra, A., Laumann, T.O., Snyder, A.Z., Schlaggar, B.L., Petersen, S.E., 2014. Methods to detect, characterize, and remove motion artifact in resting state fMRI. NeuroImage 84, 320–341. doi:10.1016/j.neuroimage.2013.08.048.

Power, J.D., Schlaggar, B.L., Petersen, S.E., 2015. Recent progress and outstanding issues in motion correction in resting state fMRI. NeuroImage 105, 536–551. doi:10.1016/j.neuroimage.2014.10.044.

Saccà, V., Sarica, A., Quattrone, A., Rocca, F., Quattrone, A., Novellino, F., 2021. Aging effect on head motion: A Machine Learning study on resting state fMRI data. Journal of Neuroscience Methods 352, 109084. doi:10.1016/j.jneumeth.2021.109084.

Satterthwaite, T.D., Wolf, D.H., Loughead, J., Ruparel, K., Elliott, M.A., Hakonarson, H., Gur, R.C., Gur, R.E., 2012. Impact of in-scanner head motion on multiple measures of functional connectivity: Relevance for studies of neurodevelopment in youth. NeuroImage 60, 623–632. doi:10.1016/j.neuroimage.2011.12.063.

Setton, R., Mwilambwe-Tshilobo, L., Girn, M., Lockrow, A.W., Baracchini, G., Hughes, C., Lowe, A.J., Cassidy, B.N., Li, J., Luh, W.M., Bzdok, D., Leahy, R.M., Ge, T., Margulies, D.S., Misic, B., Bernhardt, B.C., Stevens, W.D., Brigard, F.D., Kundu, P., Turner, G.R., Spreng, R.N., 2022. Age differences in the functional architecture of the human brain. Cerebral Cortex 33, 114–134. doi:10.1093/cercor/bhac056.

Speck, O., Hennig, J., 2001. Motion correction of parametric fMRI data from multi-slice single-shot multi-echo acquisitions. Magnetic Resonance in Medicine 46, 1023–1027. doi:10.1002/mrm.1291.

Wong, C.W., DeYoung, P.N., Liu, T.T., 2016. Differences in the resting-state fMRI global signal amplitude between the eyes open and eyes closed states are related to changes in EEG vigilance. NeuroImage 124, 24–31. doi:10.1016/j.neuroimage.2015.08.053.

Wong, C.W., Olafsson, V., Tal, O., Liu, T.T., 2013. The amplitude of the resting-state fMRI global signal is related to EEG vigilance measures. NeuroImage 83, 983–990. doi:10.1016/j.neuroimage.2013.07.057.

Yan, C.G., Cheung, B., Kelly, C., Colcombe, S., Craddock, R.C., Martino, A.D., Li, Q., Zuo, X.N., Castellanos, F.X., Milham, M.P., 2013. A comprehensive assessment of regional variation

in the impact of head micromovements on functional connectomics. NeuroImage 76, 183–201. doi:10.1016/j.neuroimage.2013.03.004.